

The impact of nanostructure on hygroscopicity and reactivity of fatty acid atmospheric aerosol proxies

Adam Milsom,¹ Adam M. Squires,² Ben Laurence,² Ben Woden,³ Andrew J. Smith,⁴ Andrew D. Ward⁵ and Christian Pfrang.^{1,6,*}

¹School of Geography, Earth and Environmental Sciences, University of Birmingham, Edgbaston, B15 2TT, Birmingham, UK.

²Department of Chemistry, University of Bath, South Building, Soldier Down Ln, Claverton Down, BA2 7AX, Bath, UK.

³Department of Chemistry, University of Reading, RG6 6AD, Reading, Berkshire, UK

⁴Diamond Light Source, Diamond House, Harwell Science and Innovation Campus, OX11 0DE, Didcot, UK.

⁵Central Laser Facility, STFC Rutherford Appleton Laboratory, Didcot OX11 0FA, UK

⁶Department of Meteorology, University of Reading, Whiteknights, Earley Gate, RG6 6BB, Reading, UK.

*Corresponding author: Professor Christian Pfrang (c.pfrang@bham.ac.uk)

Abstract

Atmospheric aerosol hygroscopicity and reactivity play key roles in determining an aerosol's fate and are strongly affected by its composition and physical properties. Fatty acids are surfactants commonly found in organic aerosol emissions. They form a wide range of different nanostructures dependent on water content and mixture composition. In this study we follow nano-structural changes in mixtures frequently found in urban organic aerosol emissions, i.e. oleic acid, sodium oleate and fructose, during humidity change and exposure to the atmospheric oxidant ozone. Addition of fructose altered the nanostructure by inducing molecular arrangements with increased surfactant-water interface curvature. Small-Angle X-ray Scattering (SAXS) was employed for the first time to derive the hygroscopicity of each nanostructure by measuring time- and humidity-resolved changes in nano-structural parameters. We found that hygroscopicity is directly linked to the specific nanostructure and is dependent on the nanostructure geometry. Reaction with ozone revealed a clear nanostructure-reactivity trend, with notable differences between the individual nanostructures investigated. Simultaneous Raman microscopy complementing the SAXS studies revealed the persistence of oleic acid even after extensive oxidation. Our findings demonstrate that self-assembly of fatty acid nanostructures can significantly impact two key atmospheric aerosol processes: water uptake and chemical reactivity, thus directly affecting the atmospheric lifetime of these materials. This could have significant impacts on both urban air quality (e.g. protecting harmful urban emissions from atmospheric degradation and therefore enabling their long-range transport), and climate (e.g. affecting cloud formation), with implications for human health and wellbeing.

Deleted: the

Introduction

Atmospheric aerosols represent a large uncertainty when considering their impact on the climate (Boucher et al., 2013; Shrivastava et al., 2017) and urban particulate matter makes a

44 significant contribution to air pollution, affecting air quality and health (Shrivastava et al., 2017;
45 Harrison, 2020; Chan and Yao, 2008; Pöschl, 2005). Organic matter can account for a large
46 portion of aerosol emissions depending on the emission source (Jimenez et al., 2009) and
47 environmental conditions have been shown to affect aerosol composition (Li et al., 2021).
48 There are both anthropogenic and biogenic sources of organic aerosols. Activities such as
49 cooking emit a range of organic compounds which can go on to form secondary organic
50 aerosol (SOA) (Zeng et al., 2020). Cooking emissions have been estimated to add ca. 10 %
51 to UK PM_{2.5} emissions (Ots et al., 2016) and have been linked with poor air quality (Stavroulas
52 et al., 2023).

Oleic acid is a fatty acid and a common organic compound found in both cooking (Zeng et al.,
53 2020; Alves et al., 2020; Vincente et al., 2018) and marine emissions (Fu et al., 2013). It is
54 reactive towards common atmospheric oxidants such as ozone and NO₃, making it a model
55 compound for laboratory studies into aerosol properties (Zahardis and Petrucci, 2007;
56 Gallimore et al., 2017; Pfrang et al., 2017; Pfrang et al., 2011; Pfrang et al., 2010; King et al.,
57 2010; Sebastiani et al., 2022; Shiraiwa et al., 2012; Shiraiwa et al., 2010). Other common
58 organic emissions are saccharides (sugars), which are also found in urban (Wang et al., 2006)
59 and biogenic emissions (Fu et al., 2013; Fu et al., 2008; Kirpes et al., 2019). Sugar emissions
60 such as levoglucosan and glucose have been shown to react readily with Criegee
61 intermediates, which are formed during ozonolysis (Enami et al., 2017). The fact that these
62 two common classes of organic compounds (fatty acids and sugars) are found in the same
63 aerosol samples raises the possibility that they are able to interact; for example by a sugar
64 reacting with oleic acid ozonolysis Criegee intermediates, potentially altering the product
65 distribution and adding to the complexity of this reaction mechanism – a possibility explored
66 in this study.

67 Aerosol phase state has been predicted to vary significantly in the atmosphere and is linked
68 to factors such as composition, humidity and temperature (Shiraiwa et al., 2017; Schmedding
69 et al., 2020). One key influence on aerosol multiphase processes is particle viscosity (Reid et
70 al., 2018) and viscous phases have been identified by field measurements of SOA (Virtanen
71 et al., 2010). Particle viscosity can vary by orders of magnitude between phase states, which
72 means the diffusion coefficients of small molecules through the particle phase also vary and
73 heterogeneous processes (*i.e.* oxidation and water uptake) are affected (Shiraiwa et al., 2011;
74 Koop et al., 2011). Viscous phases can induce diffusion gradients during particle
75 humidification (Alpert et al., 2019; Hosny et al., 2016; Renbaum-Wolff et al., 2013; Zobrist et
76 al., 2011). Particles of oleic acid have also been observed to increase in viscosity as a result
77 of oxidation (Hosny et al., 2016). The fate of organic atmospheric aerosols is therefore strongly
78 influenced by their phase state.

79 Organic coatings are present on the surface of marine aerosols, where sugars and fatty acids
80 were found to be major constituents (Kirpes et al., 2019). Poor air quality has been linked to
81 high PM_{2.5} surface organic content in Beijing, China (Zhao et al., 2020) and the long-range
82 transport of harmful substances emitted in the urban environment has been attributed to
83 viscous organic coatings and the phase state of the aerosol (Shrivastava et al., 2017; Mu et
84 al., 2018). Analysis of marine aerosols heavily influenced by anthropogenic activity found that
85 fatty acids were present along with Polycyclic Aromatic Hydrocarbons (PAHs) and phthalates,
86 which are known to cause poor health (Kang et al., 2017). There is a long-standing
87 discrepancy between the longer lifetime measured in the field compared to laboratory
88 measurements for oleic acid (Rudich et al., 2007; Wang and Yu, 2021). These observations
89 suggest that aerosols are able to travel far from their sources and that the formation of viscous
90 organic coatings could account for their long-range transport.

Deleted: Zobrist et al., 2011;

Deleted: have

94 Pure oleic acid in the liquid phase exhibits some order by the formation of dimers (Iwahashi et
 96 al., 1991). As a surfactant, the addition of its ionic form (sodium oleate) and water can induce
 the formation of lyotropic liquid crystal (LLC) phases (Tiddy, 1980). These are three-
 dimensional nanostructures which can vary from spherical and cylindrical micelles to
 bicontinuous networks and bilayers. The spherical and cylindrical micelles can exist with
"normal" (oil in water) or "inverse" (water in oil) curvature; the latter are the class formed by
the systems in this paper (Pfrang et al., 2017). In our studies, the spherical inverse micelles
 100 can exist as (disordered) "inverse micellar" phases, or as ordered "close-packed inverse
micellar" phases, which may have cubic (Fd3m) or hexagonal (P6₃/mmc) symmetry. The
 102 cylinders typically pack as hexagonal arrays ("inverse hexagonal phase") and the bilayers as
 104 "lamellar" stacks. These structures, shown in Figure 1, can be followed by Small-Angle X-ray
 Scattering (SAXS), which probes the nanometre scale. The close-packed inverse micellar,
 106 inverse hexagonal, and lamellar phases all show long-range periodicity, giving rise to Bragg
 108 peaks in SAXS patterns whose positions show symmetries and repeat spacings. The
(disordered) inverse micellar phase gives a broad hump in SAXS, whose position shifts with
micelle size.

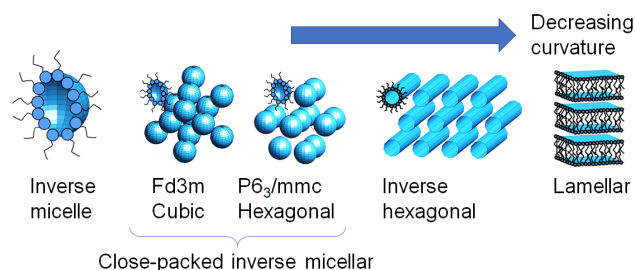


Figure 1: different phases formed by the surfactant systems in this study

110 Each of these structures exhibit varying physical properties, the key ones being diffusivity and
 112 viscosity. Diffusion coefficients can vary dramatically between micellar, close-packed micellar,
 inverse hexagonal and lamellar phases with diffusion in the latter two becoming directionally
 114 dependent (Lindblom and Orädd, 1994; Orädd et al., 1995). The diffusion of atmospherically
 relevant small molecules, such as ozone and water, would therefore also be affected by the
 nanostructure formed in the organic medium, affecting the key aerosol heterogeneous
 116 processes of water uptake and chemical reaction. While the present study is exploring the
behaviour of organic aerosol components, we acknowledge the presence of other components
 118 in atmospheric aerosols, specifically inorganic species, which can undergo efflorescence and
will add to the complexity of the behaviour of real atmospheric material compared to our
 120 organic-material focussed proxies.

122 We have previously demonstrated the feasibility of LLC formation in levitated particles of a
 fatty acid aerosol proxy (Pfrang et al., 2017; Milsom et al., 2023; Milsom et al., 2022a) and
 124 have exploited the SAXS experiment to quantify the effect of self-assembly on reaction kinetics
 (Milsom et al., 2021a), along with modelling of the potential impact on the atmospheric lifetime
 126 of LLC formation (Milsom et al., 2022b). In this study we coat capillaries with a self-assembled
 oleic acid/sodium oleate/fructose proxy use SAXS to follow changes in these nanostructures
 128 during humidity cycles and exposure to ozone. We investigate the sensitivity of the

Deleted: lamellar sheets

Deleted: [ref]

Formatted: Subscript

Deleted:

Formatted: Font: (Default) Arial

Deleted: ¶

Deleted: (cylindrical micellar)

136 nanostructure to proxy composition and humidity and demonstrate that reactivity is affected
by nanostructure.

138 **Methods**

Preparation of self-assembled coatings inside quartz capillaries

140 The method of film preparation is identical to that described in Milsom et al. (2021a). While
142 coatings inside quartz capillaries will only provide very limited insight on the behaviour of
144 coatings on aqueous droplets (which are better approximated by floating self-assembled
monolayers at the air-water interface as in previous work, e.g. Pfrang et al., 2014, Woden et
146 al., 2018 and Sebastiani et al., 2022), they are good proxies for coatings of solid particles in
the atmosphere such as mineral dust. Sample coating solutions were prepared as follows:
148 oleic acid (Sigma-Aldrich, 90 %), sodium oleate (Sigma-Aldrich, 99 %) and fructose (Sigma-
150 Aldrich, 99 %) were dissolved as 10 wt % solutions in methanol and samples weighed to the
desired ratio. All coating solutions are weighed as 1:1:x wt ratio mixtures (oleic acid:sodium
oleate:fructose), where x is 0.5, 1, 2 corresponding to 20, 33 and 50 wt % fructose
compositions.

SAXS experiment and simultaneous Raman microscopy on films coated inside quartz capillaries

152 SAXS probes aggregates at the nanometre scale, measuring order at the molecular, rather
154 than atomic (X-ray diffraction), scale (Li et al., 2016; Pauw, 2013). The scattered intensity is
156 measured against a scattering parameter (q) which is proportional to the scattering angle. q is
inversely proportional to the characteristic spacing between equivalent scattering planes (d)
via equation 1. This is also a measure of the spacings between inverse micelles.

$$158 \quad d = \frac{2\pi}{q} \quad (1)$$

160 This d -spacing can be used to determine a range of nano-structural parameters - for example,
the water layer thickness between lamellar sheets (Kulkarni et al., 2011; Milsom et al., 2022c).

162 This experimental setup is the same as used in our previous capillary film study (Milsom et al.,
2021a). Key experimental parameters are listed here: SAXS patterns were collected as 1s
164 exposures at different positions along the coated capillary with a delay of 75 s between each
scan to avoid any X-ray beam damage; the beam size at the sample was approximately 320
x 400 μm (FWHM); SAXS patterns were acquired between $q = 0.008 - 0.6 \text{ \AA}^{-1}$ by a *Pilatus*
166 *P3-2M* detector.

168 The Raman microscopy setup is as described in Milsom et al. (2021a): A 532-nm Raman laser
probe was focussed with a long working distance objective (numerical aperture: 0.42) and a
minimum spot diameter of $\sim 1.5 \mu\text{m}$. The emitted laser power was 20 – 50 mW. By following
170 the oleic acid C=C bond peak at $\sim 1650 \text{ cm}^{-1}$ and normalising to the $-\text{CH}_2$ peak at $\sim 1442 \text{ cm}^{-1}$,
we were able to follow the progress of the ozonolysis reaction simultaneous to the SAXS
172 measurements.

Controlled humidification of coated films

174 Humidity was monitored and controlled using a bespoke Raspberry Pi (RPi) system. Dry (room
air) and wet pumps were controlled by the RPi, in order to reach the target relative humidity
176 (RH), which was measured by a sensor at the outlet of the coated capillary tube with a
precision of 2 %.

178 After samples were coated, they were left for ~ 15 min to equilibrate at room humidity (~ 50 –
 180 60 % RH) before being attached to the humidity control system. The capillary was then
 182 humidified to the desired settings using the RPi control programme adjusting humidity in the
 184 range of ca. 40 to 90% RH.

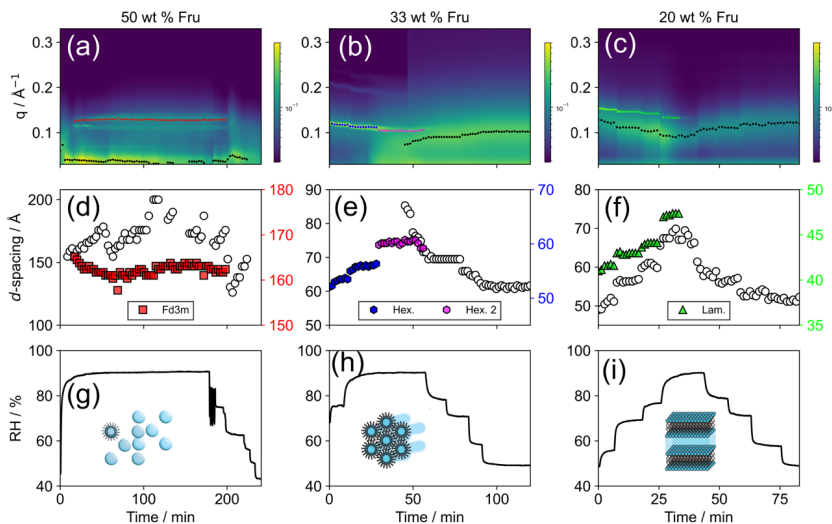
182 Ozonolysis of coated films

The ozonolysis procedure follows what was set out previously (Milsom et al., 2021a) and is
 184 summarised here: Oxygen (BOC, 99.5 %) was passed through a pen-ray ozoniser (Ultraviolet
 186 Products Ltd., Cambridge, UK) which was calibrated offline by UV spectroscopy; the ozone
 188 concentration for all ozonolysis experiments was 77 ± 5 ppm at a flow rate of 60 mL min^{-1} .
 Note that such a high ozone concentration (atmospheric ozone levels rarely exceed 0.1 ppm)
 190 was used as it is known that self-assembled semi-solid phases slow the rate of reaction
 192 significantly (Pfrang et al., 2017; Milsom et al., 2021a). Therefore, comparatively high ozone
concentrations were chosen to be able to observe an oxidative decay during the limited
timescale of synchrotron experiments while they are substantially higher than those generally
encountered in the atmosphere. The ozone-oxygen mixture was measured to be at < 5 % RH.

Film thickness was determined by X-ray beam attenuation using diodes measuring the
 194 incident and transmitted intensities. The maximum attenuation was determined by filling a
 196 capillary with sample material. The thickness of each coated film was then calibrated by
 comparison with the filled capillary's attenuation.

198 Results and Discussion

Time- and humidity-resolved nanostructure changes



200 Figure 2. (a)-(c) SAXS patterns as a function of time during the humidity cycle. Peak positions
 202 for inverse micellar (black markers) and specific nanostructures (coloured markers) are q
 204 values corresponding to the time-resolved d -spacings represented in (d)-(f). (g)-(i)
 Simultaneous RH vs time during the experiment. Each set of SAXS, d -spacing and RH data

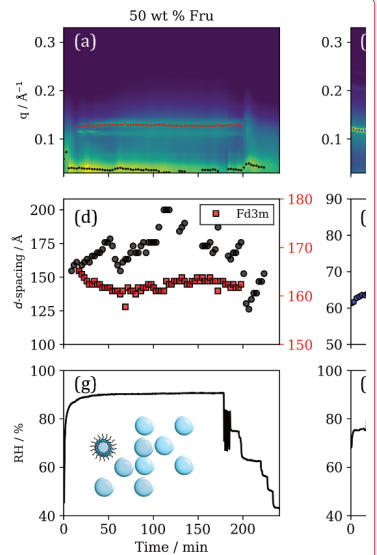
Deleted: typical atmospheric concentrations are ppb level...

Deleted: Controlled humidification of coated films

Humidity was monitored and controlled using a bespoke Raspberry Pi (RPi) system. Dry (room air) and wet pumps were controlled by the RPi, in order to reach the target relative humidity (RH), which was measured by a sensor at the outlet of the coated capillary tube with a precision of 2 %.

After samples were coated, they were left for ~ 15 min to equilibrate at room humidity (~ 50 – 60 % RH) before being attached to the humidity control system. The capillary was then humidified to the desired settings using the RPi control programme.

Deleted:



Deleted:

Deleted: 1

230 is presented for each proxy fructose composition as wt % of organic mass with oleic acid and
 232 sodium oleate in a 1:1 wt ratio: (a), (d), (g) – 50 wt %; (b), (e), (h) – 33 wt %; (c), (f), (i) – 20 wt
 234 % (i.e. 50 wt % fructose is a 1:1:2 oleic acid:sodium oleate:fructose mixture). The additional
 phases co-existing with the (disordered) inverse micellar phase are the cubic close-packed
 inverse micellar (Fd3m) phase (a,d,g); two different inverse hexagonal phases (b,e,h); and the
 lamellar phase (c,f,i).

236 Different amounts of fructose in the organic mixture result in different self-assembled
 nanostructures (Fig. 2(a)-(c)). The inverse micellar phase is seen in all experiments, and this
 238 co-exists with cubic close-packed inverse micellar, inverse hexagonal, and lamellar phases at
 50 wt% fructose, 33 wt% fructose and 20 wt% fraction, respectively. From first principles
 240 fructose, as a hydrophilic water-soluble molecule, would be expected to facilitate water uptake
 into the organic phase and act as a humectant (moisture attracting agent), analogous to the
 242 effect glycerol has on LLC phase boundaries (Richardson et al., 2015). By this logic, larger
 amounts of fructose should afford more hydrated phases at a given humidity. This can indeed
 244 be seen from a comparison of the inverse micellar spacings at high relative humidity (Figures
 2 & 3). However, this does not explain the formation of a close-packed inverse micellar phase
 246 at 50 wt% fructose vs. inverse hexagonal at 33 wt% fructose, and lamellar at 20 wt% fructose.
 We suggest that an additional effect is observed during our experiments: the water-surfactant
 248 interfacial curvature increases with increasing fructose concentration (Figure 1). This is clear
 evidence for fructose acting as a *kosmotrope* – a water-structure-inducing molecule (Kulkarni
 250 et al., 2011; Libster et al., 2008; Koynova et al., 1997). As a kosmotrope, fructose removes
 water from the water-surfactant interface. This reduces the effective surfactant headgroup
 252 area, enabling the formation of structures with increased curvature at a given water content
 (in this case, experimental humidity – see corresponding cartoons of each phase in Fig. 1).
 254 The phase boundary therefore shifts according to the amount of fructose in the mixture. A set
 of fructose content-dependent nanostructures are possible as a result. Each one of these
 256 nanostructures possesses unique physical properties (as set out in the introduction). The
 sensitivity of the nanostructure to the amount of fructose in the system suggests that the
 258 physical properties, which influence atmospheric trace gas uptake, could also change with
 similar sensitivity to aerosol composition.

260 The characteristic *d*-spacing for each of the observed nanostructures increases with
 increasing RH (Fig 2, (d)-(f)). This is the result of water filling the aqueous cavity in the inverse
 262 LLC nanostructures observed here. The time and humidity-resolved SAXS patterns acquired
 in this study have allowed us to take advantage of this characteristic and observe subtle RH-
 264 dependent changes in this parameter and directly measure the water uptake of a specific
 phase. This analysis can be applied to two coexistent phases, provided their SAXS peaks do
 266 not overlap – as is the case in our study. The effect of these phases on water uptake is
 explored in the Hygroscopicity of observed nanostructures section.

268 The phase change observed when going from low to high RH is not reversible for the two
 organic compositions which initially formed inverse hexagonal and lamellar phases at < 90 %
 270 RH (Fig. 2(b) and (c)). This suggests that the initial or final phases observed are meta-stable
 (e.g. the Fd3m and P6₃/mmc inverse micellar cubic phases can occur under the same
 272 conditions for this system; Pfrang et al., 2017). Fig. 2(d-f) shows that for a given phase
 equilibrated with water vapour at a particular RH, the *d*-spacing is stable. This suggests that
 274 these phases are in equilibrium, even if they are meta-stable.

For the 33 wt % fructose mixture, a second inverse hexagonal phase appears at high RH
 276 before eventually transitioning to an inverse micellar phase (Fig. 2(b) and (e)). Indeed,
 between ~ 40 – 60 min the inverse micellar and hexagonal phase are observed simultaneously

Deleted: 1

Deleted: u

Deleted: re

Deleted:

Deleted: (lower water-surfactant interfacial curvature)

Deleted: ,

Formatted: Font: Not Italic

Deleted: 1

Formatted: Font: Not Italic

Deleted: 1

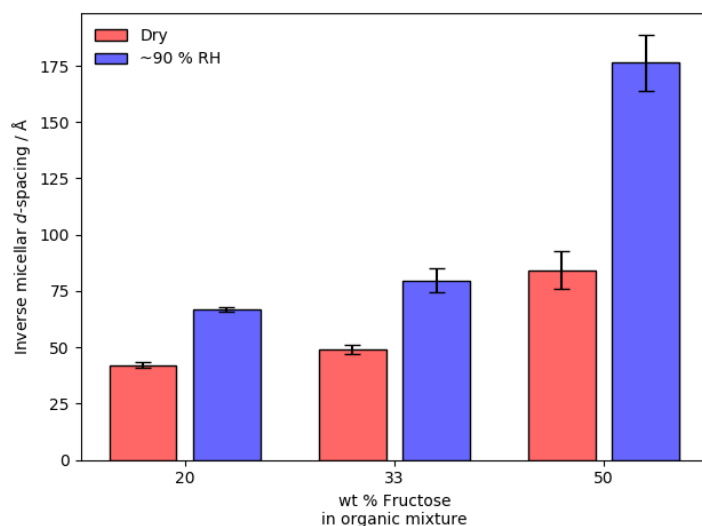
Deleted: 1

Deleted: 1

288 in the mixture. There therefore is a heterogeneity in terms of molecular order and physical
 290 properties associated with each of these nanostructures. This coexistent inverse micellar
 phase is observed for all mixtures studied here.

The 50 wt % fructose mixture exhibits a reversible phase transition from inverse micellar to a
 292 [cubic](#) close-packed inverse micellar (Fd3m) phase during a humidification-dehumidification
 cycle (Fig. 2(a)). The Fd3m phase appeared only at the highest humidity setting (90 % RH).
 294 The phase transition does not involve a significant change in phase topology, making the
 transition more facile compared with the transition to an [inverse](#) hexagonal or lamellar phase
 296 - although the Fd3m arrangement is thought to include inverse micelles of differing size
 (Seddon et al., 1990; Shearman et al., 2010).

298



300 Figure 3. Inverse micellar d -spacing vs wt % fructose in the organic mixture under dry (~ 5 %
 RH) and humid (~ 90 % RH) conditions. A clear increase in d -spacing is visible upon
 humidification of each organic film.

302 A coexistent inverse micellar phase is observed for all organic compositions during these
 humidity experiments (Fig. 2(a)-(c) – broad peak at lower q values). This coexistence
 304 represents a heterogeneity within the organic film, implying a similar heterogeneity in physical
 properties. We cannot say for certain whether this phase separation is uniform throughout the
 306 film using this technique. However, the visible shift in the inverse micellar peak position during
 humidity changes suggests that the change is happening in the majority of the film *i.e.* the
 308 inverse micellar is distributed throughout the film.

The inverse micellar d -spacing increases with the amount of fructose in the mixture under dry
 and humid conditions (Fig. 3). The inverse micellar phase observed for all fructose-containing
 310 mixtures studied here has a much larger d -spacing than mixtures without fructose, where a d -
 312 spacing of ~28-32 Å is expected (Fig. S1 – SAXS of a hydrated levitated particle of this
 composition; Mele et al., 2018). Fructose therefore stabilises larger inverse micelles. Notably,
 314 under dry (~5 % RH) conditions fructose seems to have a marked effect on the inverse micellar
 d -spacing. This implies that fructose is collecting within the inverse micellar core and that

Deleted: 1

Deleted: 2

Deleted: 1

Deleted: 2

320 possibly some water has been accommodated within the structure, explaining the increase in
the average repeat distance between inverse micelles.

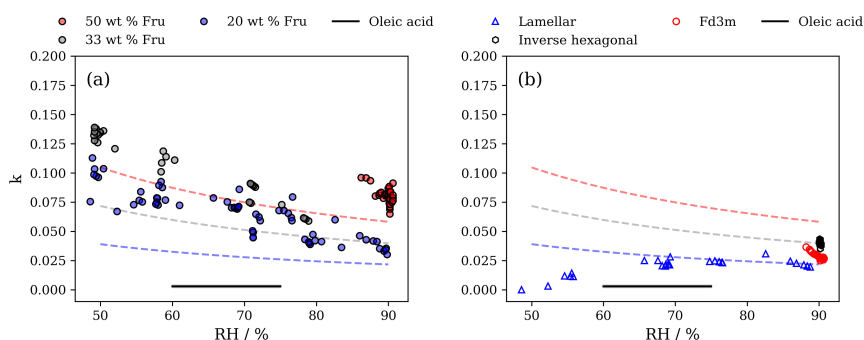
322 Increasing the humidity substantially increases the inverse micellar d -spacing for all
compositions. This effect is most potent for the 50 wt % fructose mixture (Fig. 3). The
324 observation highlights the ability of fructose to act as a humectant and stabilise large inverse
micelles. It is worth restating that these inverse micellar phases at high RH are coexistent with
326 more ordered phases. A measure of the hygroscopicity for each coexistent phase can be
extracted from the SAXS data and is presented in [the Hygroscopicity of observed
328 nanostructures section](#).

Deleted: 2

Deleted: .

330 Hygroscopicity of observed nanostructures

332 We have compared the hygroscopicity of the observed phases with what can be calculated
from Raoult's law for fructose over the RH range studied here.



334 Figure 4. Plots of hygroscopicity parameter (κ) derived from d -spacings vs RH for the inverse
micellar phases at different weight percentage fructose (wt % Fru) (a) and for other
336 nanostructures including the lamellar phase (at 20 wt % fructose), inverse hexagonal (at 33
wt % fructose) and close-packed inverse micellar (Fd3m, at 50 wt % fructose) (b). Dashed
338 lines on both plots represent κ calculated for the same fructose-lipid ratio based on Raoult's
law at a particular RH. The colours of the dashed lines correspond to the wt % fructose in the
mixture. The κ value for oleic acid measured by Rickards et al. (2013) is also plotted for
340 reference ($\kappa = 0.003 \pm 0.001$).

Deleted: 3

κ -Köhler theory derives aerosol hygroscopicity from particle sizes at different water activities
342 (a_w ; Petters and Kreidenweis, 2007). The characteristic d -spacing calculated for each
nanostructure observed here is related to its water content. We have applied κ -Köhler theory
344 by measuring the change in d -spacing with a_w , to describe the hygroscopicity of each phase.
RH was converted to a_w ($a_w = RH/100$) and it is assumed that the proxy film had equilibrated
346 with the humidity inside the capillary (see the rapid change and equilibration of the d -spacing
observed when changing RH in Fig. 2). Note that κ -Köhler theory is normally applied to aerosol
348 particles linking particle growth with humidity. Here we are not measuring individual particles,
we are measuring nanoscale changes in the structural repeat distances, which are correlated
350 with water content. Equation 2 links the dry (V_d) and water (V_w) volumes with a_w and a
hygroscopicity parameter (κ ; Petters and Kreidenweis, 2007).

Deleted: 1

$$356 \quad \frac{V_w}{V_d} = \frac{a_w}{(1-a_w)} \kappa \quad (2)$$

358 The calculation of κ is based on the geometry of each phase and the information regarding
 359 the mass and volume fractions of the lipid and water regions derivable from the equilibrium d -
 360 spacings obtained by SAXS (Asghar et al., 2015; Kulkarni et al., 2011). A detailed explanation
 of the calculation of κ is provided in the ESI.

This parameterisation of hygroscopicity is based on a simplified model which does not account
 362 for non-ideal solution behaviour. Also, these experiments are not carried out on particle
 363 ensembles or single particles, as has been the application previously (Liu et al., 2021;
 364 Rickards, 2013). As theories of hygroscopicity are in general agreement at higher a_w (RH)
 (Rickards, 2013; Clegg et al., 1998; Wexler and Clegg, 2002; Fredenslund et al., 1975;
 366 Topping et al., 2005; Zuend et al., 2008; Zuend et al., 2011), our measurements of κ at high
 367 RH (maximum 90 % RH) are the most informative. However, we caution the over-interpretation
 368 of these κ values in the context of other hygroscopicity studies due to the experimental
 differences between this study and others. These κ measurements do however provide a first
 370 insight into the hygroscopic behaviour of these nanostructures and comparison between these
 results is justified by the same method used to calculate κ .

372 The hygroscopicity of the disordered inverse micellar phase formed at each composition is
 373 higher than what is predicted by Raoult's law for fructose (Fig. 4(a)). These predictions assume
 374 that it is only the fructose that takes up water. Therefore, the formation of the inverse micellar
 nanostructure, in addition to the hygroscopicity of the fructose, increases κ beyond what would
 376 be expected from the hygroscopicity of fructose alone.

The close-packed inverse micellar phase (Fd3m symmetry) appears to be less hygroscopic
 378 than the Raoult prediction by a factor of ~ 2 at 90 % RH (Fig. 4(b)). This is in contrast to the
 disordered inverse micelles coexistent with this nanostructure (Fig. 4(a)). The key difference
 380 between the two nanostructures is that the close-packed inverse micelles are restricted in
 space. The inverse hexagonal and lamellar phases are in better agreement with Raoult's law
 382 predictions at > 85 % RH (Fig. 4(b)).

The lamellar phase appears to become much less hygroscopic at low RH. This may be
 384 because of an increase in the inter-bilayer attractive forces at lower bilayer separations and/or
 more restricted alkyl chains resulting from a more crystalline bilayer (Bahadur et al., 2019). A
 386 crystalline form of this lamellar bilayer has been observed in similar systems (Tandon et al.,
 2001; Milsom et al., 2021b).

388 As a thermodynamic parameter, κ reflects the energy changes involved in changing the nano-
 structural parameters associated with phase hydration and dehydration. For the lamellar
 390 phase, work must be done in order to overcome inter- and intra-bilayer repulsion when
 increasing and decreasing the volume of water between bilayers (Parsegian et al., 1979). To
 392 clarify, if there is attraction between bilayers, then it is easier for the lamellar phase to lose
 water (i.e. lower κ at lower humidities where there is less distance and greater attraction
 394 between bilayers). In the inverse hexagonal phase, the elastic free energy change associated
 with a change in cylindrical radius is related to a bending modulus and the curvature of the
 396 cylinder, both of which are associated with the bilayer-forming lipid and are affected by the
 addition of other interacting molecules (Chen and Rand, 1997). The close-packed inverse
 398 micellar phase is more sterically restricted than the disordered inverse micelles. The
 disordered inverse micellar phase has the least frustrated hydrocarbon tails out of the
 400 nanostructures presented here (i.e. they are not constrained close together, as is the case in
 the inverse hexagonal and lamellar phases). Removing water from inverse micelles requires
 402 more energy to do because of the increased curvature that results, explaining the increased

Deleted: 3

Deleted: 3

Deleted: 3

Deleted: 3

408 κ values for inverse micelles compared with the lamellar, inverse hexagonal and inverse cubic
close-packed phases under similar conditions. These nanostructure-specific considerations
help explain the difference between experiment and prediction.

410 All κ values derived from our SAXS data are greater than what has been measured for pure
oleic acid (Fig. 4; Rickards et al., 2013). The addition of fructose alone does not account for
412 all of the differences in κ observed between pure oleic acid, predictions based on Raoult's law
and the nanostructured fatty acid proxy. There must be an effect of the nanostructure formed
414 and this effect is most pronounced for the disordered inverse micellar phase. While the κ
values reported here are substantially (up to nearly 50 times) above those previously
416 measured for oleic acid (Rickards et al. (2013), it should be noted that κ values for highly-
CCN-active salts such as sodium chloride are still higher (between 0.5 and 1.4; Petters and
418 Kreidenweis, 2007), so that the inorganic fraction may be considerably more relevant than the
nanostructure of the organic fraction for the potential of a particle to act as a CCN when
420 considering internal mixtures of organic and inorganic materials in atmospheric particles.

Deleted: 3

Formatted: Font: (Default) Arial

Formatted: Font: (Default) Arial

Formatted: Font: (Default) Arial

422 Reactivity-nanostructure relationship

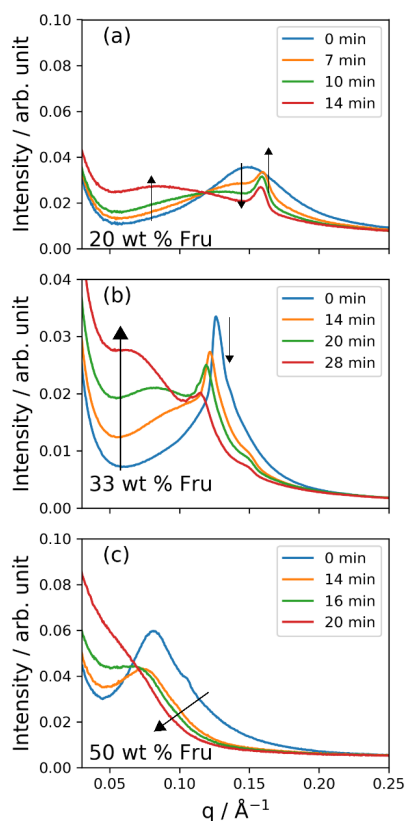


Figure 5. 1D SAXS patterns during ozonolysis of mixtures of: (a) 20 wt % fructose, (b) 33 wt % fructose and (c) 50 wt % fructose. Note the shift to low- q of the broad inverse micellar peak for each composition. An additional phase appears in the first few minutes of reaction for the 20 wt % fructose mixture (a). The additional peaks associated with the ordered inverse micellar (P6₃/mmc) are revealed after ~ 20 min for the 33 wt % fructose mixture (b) – these are indexed in the ESI. [O₃] = 77 ± 5 ppm, RH < 5 %. The black arrows indicate the progression of different peaks from ordered phases with time as a visual guide.

We subjected proxy coatings of fatty acid-fructose mixtures to ozonolysis under dry conditions analogous to our previous film kinetic study (Milsom et al., 2021a). Figure 5 presents the SAXS patterns and phases observed during ozonolysis for the fructose-containing mixtures studied here. There are broad peaks characteristic of the inverse micellar phase in all mixtures, this was the most commonly observed phase under these conditions. An extra feature from an ordered phase appears during ozonolysis for the 20 wt % fructose mixture (Fig. 5(a)) – this is discussed in conjunction with simultaneous Raman spectrometry later (see Fig. 7). An ordered phase is observed for the 33 wt % fructose film (Fig. 5(b)). Initially, the less intense peaks associated with this phase are obscured by the broad overlapping inverse micellar peak. After ~ 20 min of ozonolysis the broad peak has shifted to lower q and the other peaks are visible. These peaks index closest to a hexagonal close-packed inverse micellar phase with P6₃/mmc symmetry, which has been observed before in levitated droplets of a similar proxy (Pfrang et al., 2017) – see ESI for phase indexing. This allowed us to measure the kinetic difference between ordered and disordered inverse micellar phases.

446

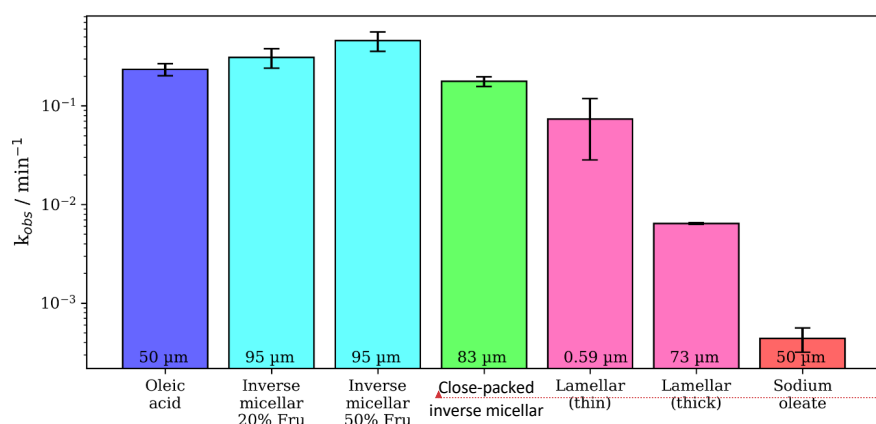


Figure 6. Pseudo-first order decay constants (k_{obs}) measured for the oleic acid-ozone reaction carried out on coated films of different composition and nanostructure. The thickness of each film is displayed at the bottom of each bar (see Table S1 in the ESI for all kinetic data and associated uncertainties). Oleic acid, sodium oleate and lamellar phase data are taken from earlier work (Milsom et al., 2021a). The lamellar phase was formed in a dry mixture of oleic acid: sodium oleate (1:1 wt). Oleic acid and sodium oleate decays were measured by following the C=C peak in the Raman spectrum as described in the methods. [O₃] = 77 ± 5 ppm and RH < 5 %.

Reaction kinetics can be followed by SAXS using an analysis technique that we have developed (Milsom et al., 2021a). We took advantage of the time resolution offered by a

Deleted: 4

Deleted: 4

Deleted: 4

Deleted: 6

Deleted: 4

Deleted: n

Deleted: ordered

Deleted:

Deleted: es

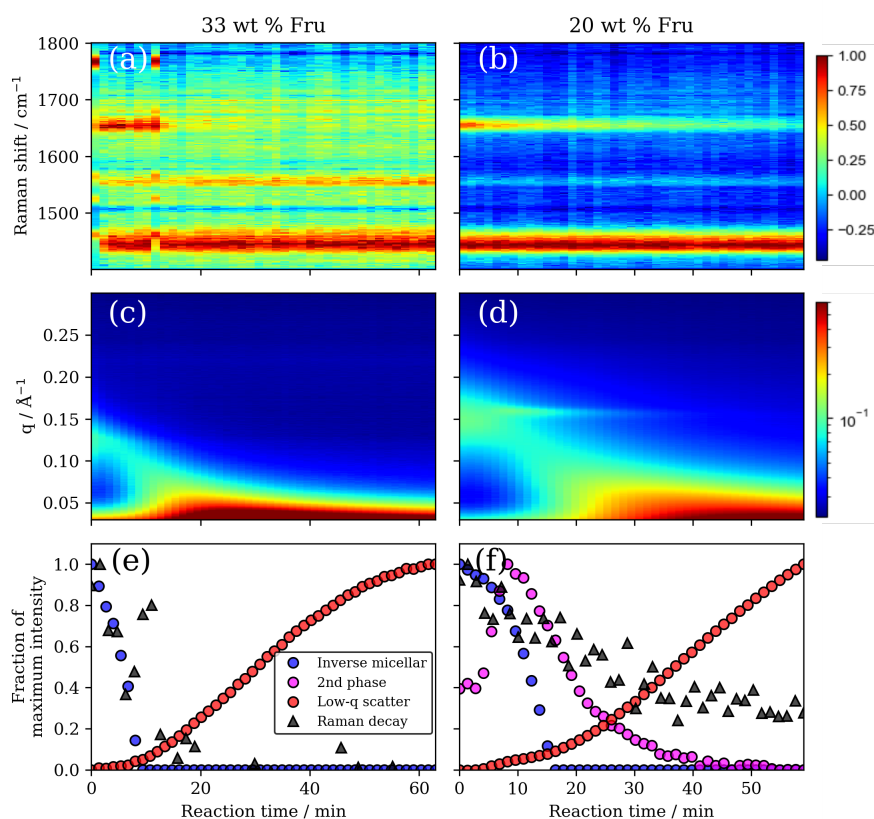
Formatted: Font: 9 pt, Font colour: Text 1

Deleted: 5

468 synchrotron experiment to derive kinetic parameters for coated organic films of different
 470 composition and nanostructure (Fig. 6). All kinetic data are summarised in Table S1 and a
 more detailed derivation of these kinetic decay parameters is presented in Milsom et al.
 (2021a).

472 The disordered inverse micellar phase reacts faster than the ordered micellar phase coated
 at a similar thickness. This is to be expected as the close-packed inverse micelles are locked
 474 into their position, increasing the viscosity of the phase and therefore slowing the diffusion of
 small molecules such as ozone. The viscosity of close-packed inverse micelles can be in the
 476 order of 10^4 times higher than for the disordered inverse micelles (Pouzot et al., 2007).

An order of reactivity exists between nanostructures. We are now able to compare the
 478 reactivity of different phases formed by this proxy system and the reactivity of its constituent
 parts (Fig. 6). Going from most to least reactive: inverse micellar > close-packed inverse
 480 micellar > (dry) lamellar. Note that the lamellar phase in this case is anhydrous. As suggested
 by Hearn *et al.*, diffusion of ozone past the closely packed lamellar chains is likely to be
 482 hindered and the rate of reaction reduced as a result, limiting the reaction to the surface of the
 film (Hearn et al., 2005).



484 Figure 7. (a) and (b) Raman spectra vs reaction time highlighting the disappearance of the
 486 oleic acid C=C peak at $\sim 1650 \text{ cm}^{-1}$ and the persistence of the $-\text{CH}_2$ deformation band at \sim

490 1442 cm⁻¹ for the 33 and 20 wt % fructose compositions, respectively. (c) and (d) simultaneous
 492 SAXS patterns vs reaction time showing the initial broad inverse micellar peak (0.12-0.15 Å⁻¹)
 494 which shifts to lower q and disappears. The increase in low- q scattering is also evident along
with the appearance of a 2nd phase peak for the 20 wt % fructose composition (d). (e) and (f)
Plots of maximum peak area intensity vs reaction time for key SAXS and Raman peaks.
Raman decay is measured by following the C=C/-CH₂ peak area ratio.

496 The close-packed (ordered) inverse micellar phase film was ~ 12 μm thinner than the inverse
 micellar films. We have shown previously that film thickness can affect reactivity (Milsom et
 498 al., 2021a), so we cannot rule out the effect of film thickness in these experiments. Though it
 was not possible to control film thickness, comparisons are still possible and actually reveal
 500 some stark differences in reactivity. Most notably is the comparison of the sub-micron lamellar
 phase film with ~ 95 μm films of inverse micellar phase. The thin lamellar phase film reacts
 502 slower than the inverse micellar films despite the ~ 160-fold difference in film thicknesses.
 There is also a difference of nearly two orders of magnitude in reactivity between the thickest
 504 lamellar film (73 μm) and the inverse micellar films (95 μm).

The inverse micellar d -spacing increases (q decreases) as ozonolysis progresses (Fig. 7).
 506 This experiment was carried out under dry conditions, so the increase in spacing must be a
 result of the reaction rather than any water uptake. We suggest that fructose itself reacts with
 508 one of the intermediate products. Common saccharides found in the atmosphere, including
 glucose (closely related to fructose), have been shown to react readily with Criegee
 510 intermediates that are formed as a result of ozonolysis (Enami et al., 2017). This forms ethers
 of greater mass and therefore products are likely to take up more space, accounting for the
 512 increase in d -spacing observed during our ozonolysis experiment. Fructose can form an ether
 with oleic acid, however, to the author's knowledge, this has only been observed as an
 514 enzymatic reaction (Ye and Hayes, 2011). Reaction with a Criegee intermediate is therefore
 the most probable explanation.

516 Products may themselves self-assemble. The increase in low- q scattering observed here was
 not observed during reactions of similar samples without fructose (Milsom et al., 2021a). This
 518 suggests that the species causing the increased low- q scatter is associated with the fructose
 in the system. If high-molecular-weight fructose products are formed, the marked increase in
 520 low- q scatter suggests that these molecules aggregate into structures with large repeat
 distances.

522 A new phase was formed with a peak in q -range of ca. 0.14–0.16 Å during the ozonolysis of
 the 20 wt % fructose mixture (Fig. 5(a) and Fig. 7(d)). This was unexpected as it was assumed
 524 that self-assembly would be destroyed by chemical reaction of the constituent fatty acid, as
 observed previously (Pfrang et al., 2017; Milsom et al., 2021a). This phase took longer to
 526 disappear compared with the initial inverse micellar phase. The reaction induced
 heterogeneity in the film both in the nanostructure and corresponding physical properties. This
 528 observation suggests that there is a dynamic relationship between nanostructure and the
 chemical reaction of this fatty acid aerosol proxy. The identity of this phase is uncertain due to
 530 the lack of a 2nd order peak in the SAXS pattern, however this peak appears where the dry
 lamellar phase peak is expected to occur (Milsom et al., 2021a; Mele et al., 2018) – this is the
 532 most likely arrangement. The atmospheric implications of the effect of nanostructure on
 reaction kinetics will be discussed in the following section.

534 There is evidence that the oleic acid double-bond persists at the end of the reaction (Fig. 7(b)).
 Simultaneous Raman spectroscopy on our deposited films shows clearly that the carbon-
 536 carbon double-bond peak associated with oleic acid is still present at the end of the reaction
 even though the initial SAXS peaks are not visible. The increase in inverse micellar d -spacing

Deleted: 44

Deleted: Figure 76. (a) and (b) Raman spectra vs reaction time highlighting the disappearance of the oleic acid C=C peak at ~ 1650 cm⁻¹ and the persistence of the -CH₂ deformation band at ~ 1442 cm⁻¹ for the 33 and 20 wt % fructose compositions, respectively. (c) and (d) simultaneous SAXS patterns vs reaction time showing the initial broad inverse micellar peak (0.12-0.15 Å⁻¹) which shifts to lower q and disappears. The increase in low- q scattering is also evident along with the appearance of a 2nd phase peak for the 20 wt % fructose composition (d). (e) and (f) Plots of maximum peak area intensity vs reaction time for key SAXS and Raman peaks. Raman decay is measured by following the C=C/-CH₂ peak area ratio. ¶

Deleted: 6

Deleted: in the

Deleted: 4

Deleted: 6

Deleted: 6

558 (SAXS peak shift to lower q), the notable increase in low- q scattering and the persistence of
 560 the double-bond suggests that oleic acid may be protected by the increase in viscosity
 562 expected by the formation of larger molecular mass molecules, which have been identified as
 564 products for the oleic acid-ozone system (Reynolds et al., 2006; Zahardis et al., 2005). This
 566 persistence is consistent with most of the recent work on coated capillaries and residues
 568 observed after oxidising monolayers of atmospheric surfactants (including oleic acid) coated
 570 on water (Milsom et al., 2021a; Woden et al., 2021; Woden et al., 2018; Sebastiani et al.,
 2022; Sebastiani et al., 2018; Pfrang et al., 2014; for completeness, it should be noted that
 King et al., 2009, also reported a residue following oleic acid ozonolysis, although this finding
 was subsequently reported to be likely caused by an impurity in the deuterated sample used
 in this early study and there was no evidence of such a residue in their most recent work, see
 King et al., 2020). This highlights the utility of a simultaneous technique to measure reaction
 kinetics (Raman spectroscopy).

Deleted: King et al., 2009;

Deleted:)

572 Atmospheric implications

574 A wide distribution of aerosol phase states in the atmosphere has been observed and
 576 predicted with global chemistry models (Shiraiwa et al., 2017; Schmedding et al., 2020;
 578 Virtanen et al., 2010). This phase state is dependent on the aerosol's environment, which
 580 includes humidity and temperature. Aerosol multiphase processes are strongly affected by the
 582 formation of semi-solid and glassy phases due to reduced gas-particle interactions and the
 584 effect on particle diffusivity (Berkemeier et al., 2016; Zhou et al. 2019; Zhou et al. 2013;
 Mikhailov et al., 2009; Koop et al., 2011; Zobrist et al., 2011). This in turn leads to phase-
 dependent increases in aerosol atmospheric lifetimes, and can facilitate the long-range
 transport of an aerosol substantially. Particle phase state and viscous aerosol organic coatings
 have been linked to the long-range transport of polycyclic aromatic hydrocarbons (PAHs),
 which are particularly harmful to human health by acting as carcinogens (Shrivastava et al.,
 2017; Mu et al., 2018).

Deleted: ,

586 In the work presented here, we are adding a further organic aerosol component to our bottom-
 588 up approach for this fatty acid aerosol proxy system with the addition of the sugar fructose,
 which is commonly found in urban and marine emissions. The addition of fructose induces
 nano-structural changes by acting as a kosmotrope under humidified conditions. This shows
 that the nanostructure depends on the organic composition in addition to the relative humidity.
 590 The presence of other aerosol components will likely impact the self-assembly reported here,
 592 but, we expect that fatty acid self-assembly still occurs in their presence as briefly outlined
 594 below (compare discussion in Pfrang et al., 2017). Uncharged water-soluble components have
 596 been shown to dissolve in the aqueous region of the self-assembled structure, acting as a
 598 humectant (in addition to the role as kosmotrope demonstrated for fructose in the present
 work), and allowing the self-assembly to occur at lower humidities. Charged water-soluble
 inorganic components will have the same effect, but in addition, by changing the ionic strength
 and head group charge, will shift the phase boundaries between different self-assembled
 structures. Hydrophobic aerosol components will partition into the non-aqueous regions of the
 self-assembled phases promoting the formation of inverse ('water-in-oil') phases.

Formatted: Font: (Default) Arial, Not Italic

Formatted: Font: (Default) Arial, Not Italic

600 In this study, we quantify two key properties affected by the nanostructure: hygroscopicity and
 602 reactivity. As illustrated in Fig. 4, the nanostructure increases the hygroscopicity parameter (κ)
 604 by as much as a factor of ca. 10 to 50 compared to liquid oleic acid. Hygroscopicity determines
 the water uptake of aerosol at a specific RH; we have previously shown (Milsom et al., 2022a)
 that aerosol water content strongly impacts on viscosity. Fig. 6 shows that the aerosol
 reactivity changes by nearly two orders of magnitude when altering the nano-structural

Deleted:

Deleted: ¶

Deleted: 3

Deleted:

Deleted: ¶

Deleted: 5

arrangement e.g. between a 73- μm thick lamellar film and a 95- μm thick inverse micellar film. This strong effect on aerosol reactivity associated with the nanostructure is likely due to changes in viscosity and diffusivity. We acknowledge that the film thicknesses given in Fig. 6 are comparatively thick considering that most atmospheric aerosols accumulate in the 0.1–2.5- μm range. However, as discussed in Pfrang et al. (2017), for thermodynamically equilibrated phases, no substantial size dependence is expected and we could confirm consistent self-assembly from 500-nm films to 2-mm droplets, i.e. covering the key size range for atmospheric particles. If some of the phases identified in our atmospheric aerosol proxy were not thermodynamically stable states, the exact phase observed at a given point in the experiment would depend on timescales and therefore droplet size/film thickness, but complex self-assembly would still be expected to occur. In Milsom et al. (2021) we have reported the film thickness-dependent kinetic behaviour and measured the effect of the organic phase on the kinetics.

Deleted: of nanostructure

Formatted: Font: (Default) Arial, Not Italic

Previously, we have shown that ozonolysis destroys self-assembly in fatty acid aerosol proxies (Pfrang et al., 2017; Milsom et al., 2021a). Here we additionally show that ozonolysis can induce the formation of a new intermediate molecular arrangement (see Fig. 7(d)), demonstrating the possibility that self-assembly could be induced by the chemical reaction of these atmospheric molecules with ozone. This, in combination with humidity-induced phase changes, suggests a dynamic aerosol phase state which is dependent on the molecular arrangement of the surfactant molecules.

Deleted: 6

Atmospheric aerosols exhibit heterogeneity both in terms of composition and physical properties (Kirpes et al., 2019; Schill et al., 2015). Particle viscosity can become heterogeneous during chemical reaction and exposure to humidity (Hosny et al., 2016). We have now demonstrated that nano-structural heterogeneity exists during humidity change and ozonolysis where different nanostructures coexist. There must therefore be a heterogeneity in hygroscopicity in our proxy films due to the link between nanostructure and κ (see Fig. 4). The formation of an intermediate nanostructure during ozonolysis observed here suggests that viscosity may not be equal throughout the film and that the diffusivity of small molecules such as ozone throughout the particle would also not be uniform, affecting the lifetime of the proxy (Shiraiwa et al., 2011b). The increase in d -spacing we observed between inverse micelles during ozonolysis suggests that larger molecules are formed as a result of the reaction (see Fig. 5 and Fig. 7(c) & (d)). These larger molecules may also contribute to film heterogeneity and alter the reactive lifetime of these molecules.

Deleted: 3

Deleted: 4

Deleted: 6

Sugars and fatty acids, such as fructose and oleic acid, are commonly encountered components of aerosols emitted in urban (Wang et al., 2006) and marine (Fu et al., 2013) environments. Specifically, saccharides (sugars) have been identified along with fatty acids as major components of thick (μm -scale) organic coatings observed on sea spray aerosols (Kirpes et al., 2019) and also in a cafeteria environment (Alves et al., 2020), demonstrating the wide range of environments our proxies represent. Their relative abundances can vary significantly depending on season, time of day and location. In this study we have shown that the proxy sugar content has a substantial impact on aerosol physical properties via a change in nanostructure. We conclude that, as the relative amount of sugar and fatty acid changes between environments, nanostructures could also vary depending on the location and emission type.

We have now demonstrated that the reactivity of surface-active oleic acid depends not only on whether it is self-assembled (Pfrang et al., 2017; Milsom et al., 2021a), but also on the specific nanostructure it adopts (see Fig. 7). Our results suggest that the lifetime of surfactant material would depend on nanostructure, which in turn is linked to aerosol composition and

Deleted: 5

670 which is also affected by relative humidity. We would expect complex behaviour associated
 672 with humidity changes given that nanostructure both influences and is influenced by humidity.
 674 The associated surfactant lifetime will also change. It should be noted that we have carried
 676 out the ozonolysis experiments presented here only at low humidity and at high ozone levels;
 678 the possible implications of this deviation from atmospheric conditions would merit further
 680 investigation (noting experimental challenges associated with interfering reactions of highly
 682 reactive OH radicals potentially produced in ozonolysis studies at high humidities). Our earlier
 684 modelling work (Milsom et al., 2022b) estimated significantly extended half-lives of
 686 nanostructured (lamellar-phase) oleic acid for a range of atmospherically relevant film
 688 thicknesses and ozone levels (e.g. a half-life increase of ca. 10 days for a 0.75 µm film in ca.
 690 25 ppb ozone; see Fig. 7 in Milsom et al., 2022b). The persistence of surface-active material
 has been demonstrated experimentally at the air-water interface (Woden et al., 2021; Woden
 et al., 2018; Sebastiani et al., 2022; Sebastiani et al., 2018; Pfrang et al., 2014). Simultaneous
 Raman microscopy suggests that oleic acid can persist in the films studied here, a finding
 consistent with non-fructose-containing films of this proxy (Milsom et al., 2021a). We have
 demonstrated that the reactive lifetime of oleic acid can vary by orders of magnitude as a result
 of different molecular arrangements. There is a link between surfactant content and cloud
 droplet formation potential as a result of a reduction in surface tension (Bzdek et al., 2020;
 Ovadnevaite et al., 2017; Facchini et al., 2000; Facchini et al., 1999). Therefore, any increase
 in surfactant lifetime would imply a similar increase of the cloud formation potential of a
 surfactant-containing aerosol, such as aerosols emitted from cooking or sea spray containing
 oleic acid and/or related species.

Deleted: King et al., 2009;

Deleted:

692 Conclusions

694 Our work has clearly shown that changes in the nanostructure, induced by humidity changes,
 can directly affect both water uptake and reactivity which are known to be two key aerosol
 ageing processes. e.g. Pöschl, 2005

696 Crucially, we have demonstrated and quantified the direct link between the nanostructures
 698 formed by fructose-containing fatty acid mixtures and the key aerosol properties of
 hygroscopicity and reactivity for the first time by utilising synchrotron SAXS and complimentary
 Raman microscopy. This combination of SAXS and Raman data allowed us to infer key
 700 atmospheric aerosol properties and extract information from coexistent nanostructures to draw
 comparisons between these. As a result, heterogeneity could be revealed during humidity
 702 exposure and ozonolysis. Our findings demonstrate that self-assembly of fatty acid
 nanostructures can alter both water uptake and chemical reactivity. We have also shown that
 704 ozonolysis can induce the formation of a new intermediate molecular arrangement,
 706 demonstrating the possibility that self-assembly could be induced by the chemical reaction of
these atmospheric components with ozone. This, in combination with humidity-induced phase
 708 changes, suggests a dynamic aerosol phase state which is dependent on the molecular
arrangement of the surfactant molecules.

Deleted: massively

Deleted: , with significant impacts on (i) urban air quality by protecting harmful urban emissions from atmospheric degradation and therefore enabling their long-range transport; and (ii) climate by affecting cloud formation. This could have fundamental implications for human health and wellbeing.

Formatted: Font colour: Text 1

710 Our work demonstrated the fundamental effects of nanostructure on water uptake and
 712 reactivity. While these parameters in turn affect the particles' impacts on air quality and
climate, a direct assessment of these effects is not within the scope of the work presented
here.

Formatted: Font colour: Auto

714 Data access statement

724 Data supporting with this study are available in the supporting information and from the
 725 corresponding author upon request.

726

Conflicts of interest

728 There are no conflicts to declare.

Deleted: ¶

Acknowledgements

730 This work was carried out with the support of the Diamond Light Source (DLS), instrument I22
 732 (proposal SM21663). AM wishes to acknowledge funding from NERC SCENARIO DTP award
 734 number NE/L002566/1 and CENTA DTP. The work was supported by NERC (research grant
 736 NE/T00732X/1). The authors would like to thank Nick Terrill (DLS), Tim Snow (DLS) and Lee
 738 Davidson (DLS) for technical support during beamtime experiments; Jacob Boswell is
 acknowledged for help at beamtimes. The authors are grateful to the Central Laser Facility for
 access to key equipment for the Raman work simultaneously to the DLS beamtime
 experiments.

References

- 742 Alpert, P. A., P. C. Arroyo, J. Dou, U. K. Krieger, S. S. Steimer, J.-D. Förster, F. Ditas, C.
 743 Pöhlker, S. Rossignol, M. Passananti, S. Perrier, C. George, M. Shiraiwa, T.
 744 Berkemeier, B. Watts and M. Ammann. *Phys. Chem. Chem. Phys.*, 2019, **21**, 20613–
20627.
- 746 Alves, C. A., E. D. Vicente, M. Evtugina, A. M. Vicente, T. Nunes, F. Lucarelli, G. Calzolari,
 S. Nava, A. I. Calvo, C. del B. Alegre, F. Oduber, A. Castro and R. Fraile, *Atmos.*
Pollut. Res., 2020, **11**, 531–544.
- 748 Asghar, K. A., D. A. Rowlands, J. M. Elliott and A. M. Squires, *ACS Nano*, 2015, **9**, 10970–
 10978.
- 750 Bahadur, J., A. Das and D. Sen, *J. Appl. Crystallogr.*, 2019, **52**, 1169–1175.
- 752 Berkemeier, T., S. S. Steimer, U. K. Krieger, T. Peter, U. Pöschl, M. Ammann and M.
 Shiraiwa, *Phys. Chem. Chem. Phys.*, 2016, **18**, 12662–12674.
- 754 Boucher, O., D. Randall, P. Artaxo, C. Bretherton, G. Feingold, P. Forster, V.-M. Kerminen,
 Y. Kondo, H. Liao, U. Lohmann, P. Rasch, S. K. Satheesh, S. Sherwood, B. Stevens
 and X. Y. Zhang, in *Climate Change 2013 - The Physical Science Basis*, ed.
 756 Intergovernmental Panel on Climate Change, Cambridge University Press,
 Cambridge, 2013, pp. 571–658.
- 758 Bzdek, B. R., J. P. Reid, J. Malila and N. L. Prisle, *Proc. Natl. Acad. Sci. U. S. A.*, 2020, **117**,
 8335–8343.
- 760 Chan, C. K. and X. Yao, *Atmos. Environ.*, 2008, **42**, 1–42.
- Chen, Z. and R. P. Rand, *Biophys. J.*, 1997, **73**, 267–276.
- 762 Clegg, S. L., P. Brimblecombe and A. S. Wexler, *J. Phys. Chem. A*, 1998, **102**, 2155–2171.
- Enami, S., M. R. Hoffmann and A. J. Colussi, *J. Phys. Chem. Lett.*, 2017, **8**, 3888–3894.
- 764 Facchini, M. C., S. Decesari, M. Mircea, S. Fuzzi and G. Loglio, *Atmos. Environ.*, 2000, **34**,

Formatted: Font: Italic

Formatted: Font: Bold

- 766 4853–4857.
- Facchini, M. C., M. Mircea, S. Fuzzi and R. J. Charlson, *Nature*, 1999, **401**, 257–259.
- 768 Fredenslund, A., R. L. Jones and J. M. Prausnitz, *AIChE J.*, 1975, **21**, 1086–1099.
- Fu, P. Q., K. Kawamura, J. Chen, B. Charrière and R. Sempéré, *Biogeosciences*, 2013, **10**,
770 653–667.
- Fu, P., K. Kawamura, K. Okuzawa, S. G. Aggarwal, G. Wang, Y. Kanaya and Z. Wang, *J.*
772 *Geophys. Res. Atmos.*, 2008, **113**, 1–20.
- Gallimore, P. J., P. T. Griffiths, F. D. Pope, J. P. Reid and M. Kalberer, *J. Geophys. Res.*,
774 2017, **122**, 4364–4377.
- Harrison, R. M. *Philos. Trans. R. Soc. A Math. Phys. Eng. Sci.*, 2020, **378**, 20190319.
- 776 Hearn, J. D., G. D. Smith and A. J. Lovett, *Phys. Chem. Chem. Phys.*, 2005, **7**, 501–511.
- Hosny, N. A., C. Fitzgerald, A. Vyšniauskas, A. Athanasiadis, T. Berkemeier, N. Uygur, U.
778 Pöschl, M. Shiraiwa, M. Kalberer, F. D. Pope and M. K. Kuimova, *Chem. Sci.*, 2016,
7, 1357–1367.
- 780 Iwahashi, M., Y. Yamaguchi, T. Kato, T. Horiuchi, I. Sakurai and M. Suzuki, *J. Phys. Chem.*,
1991, **95**, 445–451.
- 782 Jimenez, J. L., M. R. Canagaratna, N. M. Donahue, A. S. H. Prevot, Q. Zhang, J. H. Kroll, P.
F. DeCarlo, J. D. Allan, H. Coe, N. L. Ng, A. C. Aiken, K. S. Docherty, I. M. Ulbrich, A.
784 P. Grieshop, A. L. Robinson, J. Duplissy, J. D. Smith, K. R. Wilson, V. A. Lanz, C.
Hueglin, Y. L. Sun, J. Tian, A. Laaksonen, T. Raatikainen, J. Rautiainen, P.
786 Vaattovaara, M. Ehn, M. Kulmala, J. M. Tomlinson, D. R. Collins, M. J. Cubison, J.
Dunlea, J. A. Huffman, T. B. Onasch, M. R. Alfarra, P. I. Williams, K. Bower, Y.
788 Kondo, J. Schneider, F. Drewnick, S. Borrmann, S. Weimer, K. Demerjian, D.
Salcedo, L. Cottrell, R. Griffin, A. Takami, T. Miyoshi, S. Hatakeyama, A. Shimono, J.
790 Y. Sun, Y. M. Zhang, K. Dzepina, J. R. Kimmel, D. Sueper, J. T. Jayne, S. C.
Herndon, A. M. Trimborn, L. R. Williams, E. C. Wood, A. M. Middlebrook, C. E. Kolb,
792 U. Baltensperger and D. R. Worsnop, *Science (80-.)*, 2009, **326**, 1525–1529.
- Kang, M., F. Yang, H. Ren, W. Zhao, Y. Zhao, L. Li, Y. Yan, Y. Zhang, S. Lai, Y. Zhang, Y.
794 Yang, Z. Wang, Y. Sun and P. Fu, *Sci. Total Environ.*, 2017, **607–608**, 339–350.
- 796 King, M. D., S. H. Jones, C. O. M. Lucas, K. C. Thompson, A. R. Rennie, A. D. Ward, A. A.
Marks, F. N. Fisher, C. Pfrang, A. V. Hughes and R. A. Campbell, *Phys. Chem.*
Chem. Phys., 2020, **22**, 28032.
- 798 King, M. D., A. R. Rennie, C. Pfrang, A. V. Hughes and K. C. Thompson, *Atmos. Environ.*,
2010, **44**, 1822–1825.
- 800 King, M. D., A. R. Rennie, K. C. Thompson, F. N. Fisher, C. C. Dong, R. K. Thomas, C.
Pfrang and A. V. Hughes, *Phys. Chem. Chem. Phys.*, 2009, **11**, 7699–7707.
- 802 Kirpes, R. M., D. Bonanno, N. W. May, M. Fraund, A. J. Barget, R. C. Moffet, A. P. Ault and
K. A. Pratt, *ACS Cent. Sci.*, 2019, **5**, 1760–1767.
- 804 Koop, T., J. Bookhold, M. Shiraiwa and U. Pöschl, *Phys. Chem. Chem. Phys.*, 2011, **13**,
19238–19255.
- 806 Koynova, R., J. Brankov and B. Tenchov, *Eur. Biophys. J.*, 1997, **25**, 261–274.
- Kulkarni, C. V., W. Wachter, G. Iglesias-Salto, S. Engelskirchen and S. Ahualli, *Phys. Chem.*
808 *Chem. Phys.*, 2011, **13**, 3004–3021.

Formatted: Font: Italic

Formatted: Font: Bold

- 810 Li, G., H. Su, N. Ma, J. Tao, Y. Kuang, Q. Wang, J. Hong, Y. Zhang, U. Kuhn, S. Zhang, X.
Pan, N. Lu, M. Tang, G. Zheng, Z. Wang, Y. Gao, P. Cheng, W. Xu, G. Zhou, C.
812 Zhao, B. Yuan, M. Shao, A. Ding, Q. Zhang, P. Fu, Y. Sun, U. Pöschl and Y. Cheng,
Faraday Discuss., 2021, DOI:10.1039/D0FD00099J.
- Li, T., A. J. Senesi and B. Lee, *Chem. Rev.*, 2016, **116**, 11128–11180.
- 814 Libster, D., P. Ben Ishai, A. Aserin, G. Shoham and N. Garti, *Langmuir*, 2008, **24**, 2118–
2127.
- 816 Lindblom, G. and G. Orädd, *Prog. Nucl. Magn. Reson. Spectrosc.*, 1994, **26**, 483–515.
- Liu, J., F. Zhang, W. Xu, L. Chen, J. Ren, S. Jiang, Y. Sun and Z. Li, *J. Geophys. Res.*
818 *Atmos.*, 2021, **126**, 1–11.
- Mele, S., O. Söderman, H. Ljusberg-Wahrén, K. Thuresson, M. Monduzzi and T. Nylander,
820 *Chem. Phys. Lipids*, 2018, **211**, 30–36.
- Mikhailov, E., S. Vlasenko, S. T. Martin, T. Koop and U. Pöschl, *Atmos. Chem. Phys.*, 2009,
822 **9**, 9491–9522.
- Milsom, A., A. M. Squires, A. D. Ward and C. Pfrang, *Acc. Chem. Res.*, 2023, **56**, 2555–
824 2568.
- Milsom, A., A. M. Squires, I. Quant, N. J. Terrill, S. Huband, B. Woden, E. R. Cabrera-
826 Martinez and C. Pfrang, *J. Phys. Chem. A*, 2022a, **126**, 7331–7341.
- Milsom, A., A. M. Squires, A. D. Ward and C. Pfrang, *Atmos. Chem. Phys.*, 2022b, **22**,
828 4895–4907.
- Milsom, A., A. M. Squires, M. W. A. Skoda, P. Gutfreund, E. Mason, N. J. Terrill and C.
830 Pfrang, *Environ. Sci. Atmos.*, 2022c, **2**, 964–977.
- Milsom, A., A. M. Squires, B. Woden, N. J. Terrill, A. D. Ward and C. Pfrang, *Faraday*
832 *Discuss.*, 2021a, **226**, 364–381.
- Milsom, A., A. M. Squires, J. A. Boswell, N. J. Terrill, A. D. Ward and C. Pfrang, *Atmos.*
834 *Chem. Phys.*, 2021b, **21**, 15003–15021, doi.org/10.5194/acp-21-15003-2021.
- Mu, Q., M. Shiraiwa, M. Octaviani, N. Ma, A. Ding, H. Su, G. Lammel, U. Pöschl and Y.
836 Cheng, *Sci. Adv.*, 2018, **4**, eaap7314.
- Orädd, G., G. Lindblom, K. Fontell and H. Ljusberg-Wahren, *Biophys. J.*, 1995, **68**, 1856–
838 1863.
- Ots, R., M. Vieno, J. D. Allan, S. Reis, E. Nemitz, D. E. Young, H. Coe, C. Di Marco, A.
840 Detournay, I. A. Mackenzie, D. C. Green and M. R. Heal, *Atmos. Chem. Phys.*, 2016,
16, 13773–13789.
- 842 Ovadnevaite, J., A. Zuend, A. Laaksonen, K. J. Sanchez, G. Roberts, D. Ceburnis, S.
Decesari, M. Rinaldi, N. Hodas, M. C. Facchini, J. H. Seinfeld and C. O'Dowd, *Nature*,
844 2017, **546**, 637–641.
- Parsegian, V. A., N. Fuller and R. P. Rand, *Proc. Natl. Acad. Sci. U. S. A.*, 1979, **76**, 2750–
846 2754.
- Pauw, B. R. *J. Phys. Condens. Matter*, 2013, **25**, 383201.
- 848 Petters, M. D. and S. M. Kreidenweis, *Atmos. Chem. Phys.*, 2007, **7**, 1961–1971.
- Pfrang, C., K. Rastogi, E. R. Cabrera-Martinez, A. M. Seddon, C. Dicko, A. Labrador, T. S.
850 Plivelic, N. Cowieson and A. M. Squires, *Nat. Commun.*, 2017, **8**, 1724.

- 852 Pfrang, C., F. Sebastiani, C. O. M. Lucas, M. D. King, I. D. Hoare, D. Chang and R. A. Campbell, *Phys. Chem. Chem. Phys.*, 2014, **16**, 13220–13228.
- Pfrang, C., M. Shiraiwa and U. Pöschl, *Atmos. Chem. Phys.*, 2011, **11**, 7343–7354.
- 854 Pfrang, C., M. Shiraiwa and U. Pöschl, *Atmos. Chem. Phys.*, 2010, **10**, 4537–4557.
- Pöschl, U. *Angew. Chemie Int. Ed.*, 2005, **44**, 7520–7540.
- 856 Pouzot, M., R. Mezzenga, M. Leser, L. Sagalowicz, S. Guillote and O. Glatter, *Langmuir*, 2007, **23**, 9618–9628.
- 858 Reid, J. P., A. K. Bertram, D. O. Topping, A. Laskin, S. T. Martin, M. D. Petters, F. D. Pope and G. Rovelli, *Nat. Commun.*, 2018, **9**, 1–14.
- 860 Renbaum-Wolff, L., J. W. Grayson, A. P. Bateman, M. Kuwata, M. Sellier, B. J. Murray, J. E. Shilling, S. T. Martin and A. K. Bertram, *Proc. Natl. Acad. Sci.*, 2013, **110**, 8014–8019.
- 862 Reynolds, J. C., D. J. Last, M. McGillen, A. Nijs, A. B. Horn, C. Percival, L. J. Carpenter and A. C. Lewis, *Environ. Sci. Technol.*, 2006, **40**, 6674–6681.
- 864 Richardson, S. J., P. A. Staniec, G. E. Newby, J. L. Rawle, A. R. Slaughter, N. J. Terrill, J. M. Elliott and A. M. Squires, *Chem. Commun.*, 2015, **51**, 11386–11389.
- 866 Rickards, A. M. J., R. E. H. Miles, J. F. Davies, F. H. Marshall and J. P. Reid, *J. Phys. Chem. A*, 2013, **117**, 14120–14131.
- 868 Rudich, Y., N. M. Donahue and T. F. Mentel, *Annu. Rev. Phys. Chem.*, 2007, **58**, 321–352.
- Schill, S. R., D. B. Collins, C. Lee, H. S. Morris, G. A. Novak, K. A. Prather, P. K. Quinn, C. M. Sultana, A. V. Tivanski, K. Zimmermann, C. D. Cappa and T. H. Bertram, *ACS Cent. Sci.*, 2015, **1**, 132–141.
- 872 Schmedding, R., Q. Z. Rasool, Y. Zhang, H. O. T. Pye, H. Zhang, Y. Chen, J. D. Surratt, F. D. Lopez-Hilfiker, J. A. Thornton, A. H. Goldstein and W. Vizuete, *Atmos. Chem. Phys.*, 2020, **20**, 8201–8225.
- 874 Sebastiani, F., R. A. Campbell and C. Pfrang, *Environ. Sci.: Atmos.*, 2022, **2**, 1324–1337.
- 876 Sebastiani, F., R. A. Campbell, K. Rastogi and C. Pfrang, *Atmos. Chem. Phys.*, 2018, **18**, 3249–3268.
- 878 Seddon, J. M., E. A. Bartle and J. Mingins, *J. Phys. Condens. Matter*, 1990, **2**, SA285–SA290.
- 880 Shearman, G. C., A. I. I. Tyler, N. J. Brooks, R. H. Templer, O. Ces, R. V. Law and J. M. Seddon, *Liq. Cryst.*, 2010, **37**, 679–694.
- 882 Shiraiwa, M., Y. Li, A. P. Tsimpidi, V. A. Karydis, T. Berkemeier, S. N. Pandis, J. Lelieveld, T. Koop and U. Pöschl, *Nat. Commun.*, 2017, **8**, 1–7.
- 884 Shiraiwa, M., C. Pfrang, T. Koop and U. Pöschl, *Atmos. Chem. Phys.*, 2012, **12**, 2777–2794.
- 886 Shiraiwa, M., M. Ammann, T. Koop and U. Pöschl, *Proc. Natl. Acad. Sci. U. S. A.*, 2011a, **108**, 11003–11008.
- 888 Shiraiwa, M., M. Ammann, T. Koop and U. Pöschl, *Proc. Natl. Acad. Sci. USA*, 2011b, **108**, 11003–11008, Supplementary material: DOI:10.1073/pnas.1103045108/-/DCSupplemental.
- 890 Shiraiwa, M., C. Pfrang and U. Pöschl, *Atmos. Chem. Phys.*, 2010, **10**, 3673–3691.
- Shrivastava, M., C. D. Cappa, J. Fan, A. H. Goldstein, A. B. Guenther, J. L. Jimenez, C.

- 892 Kuang, A. Laskin, S. T. Martin, N. L. Ng, T. Petaja, J. R. Pierce, P. J. Rasch, P.
894 Roldin, J. H. Seinfeld, J. Shilling, J. N. Smith, J. A. Thornton, R. Volkamer, J. Wang,
D. R. Worsnop, R. A. Zaveri, A. Zelenyuk and Q. Zhang, *Rev. Geophys.*, 2017a, **55**,
509–559.
- 896 Shrivastava, M., S. Lou, A. Zelenyuk, R. C. Easter, R. A. Corley, B. D. Thrall, P. J. Rasch, J.
D. Fast, S. L. M. Simonich, H. Shen and S. Tao, *Proc. Natl. Acad. Sci. U. S. A.*,
898 2017b, **114**, 1246–1251.
- Stavroulas, I., A. Bougiatioti, G. Grivas, E. Liakakou, K. Petrinoli, K. Kourtidis, E.
900 Gerasopoulos and N. Mihalopoulos, *Sci. Total Environ.*, 2023,
DOI:10.1016/j.scitotenv.2023.168031.
- 902 Tandon, P., S. Raudenkolk, R. H. H. Neubert, W. Rettig and S. Wartewig, *Chem. Phys.*
Lipids, 2001, **109**, 37–45.
- 904 Tiddy, G. J. T., *Phys. Rep.*, 1980, **57**, 1–46.
- Topping, D. O., G. B. McFiggans and H. Coe, *Atmos. Chem. Phys.*, 2005, **5**, 1205–1222.
- 906 Vicente, E. D., A. Vicente, M. Evtugina, R. Carvalho, L. A. C. Tarelho, F. I. Oduber and C.
Alves, *Fuel Process. Technol.*, 2018, **176**, 296–306.
- 908 Virtanen, A., J. Joutsensaari, T. Koop, J. Kannosto, P. Yli-Pirilä, J. Leskinen, J. M. Mäkelä, J.
K. Holopainen, U. Pöschl, M. Kulmala, D. R. Worsnop and A. Laaksonen, *Nature*,
910 2010, **467**, 824–827.
- Wang, Q. and J. Z. Yu, *Geophys. Res. Lett.*, 2021, DOI:10.1029/2021GL095130.
- 912 Wang, G., K. Kawamura, L. Shuncheng, K. Ho and J. Cao, *Environ. Sci. Technol.*, 2006, **40**,
4619–4625.
- 914 Wexler, A. S. and S. L. Clegg, *J. Geophys. Res.*, 2002, **107**, 4207.
- Woden, B., M. W. A. Skoda, A. Milsom, C. Gubb, A. Maestro, J. Tellam and C. Pfrang,
916 *Atmos. Chem. Phys.*, 2021, **21**, 1325–1340.
- Woden, B., M. Skoda, M. Hagreen and C. Pfrang, *Atmosphere (Basel)*, 2018, **9**, 471.
- 918 Ye, R. and D. G. Hayes, *JAOCS, J. Am. Oil Chem. Soc.*, 2011, **88**, 1351–1359.
- Zahardis, J. and G. A. Petrucci, *Atmos. Chem. Phys.*, 2007, **7**, 1237–1274.
- 920 Zahardis, J., B. W. LaFranchi and G. A. Petrucci, *J. Geophys. Res. D Atmos.*, 2005, **110**, 1–
10.
- 922 Zeng, J., Z. Yu, M. Mekic, J. Liu, S. Li, G. Loisel, W. Gao, A. Gandolfo, Z. Zhou, X. Wang, H.
Herrmann, S. Gligorovski and X. Li, *Environ. Sci. Technol. Lett.*, 2020, **7**, 76–81.
- 924 Zhao, Y., H. Huang, Y. Zhang, K. Wu, F. Zeng, J. Wang, X. Yu, Z. Zhu, X.-Y. Yu and F.
Wang, *Atmos. Environ.*, 2020, **220**, 117090.
- 926 Zhou, S., B. C. H. Hwang, P. S. J. Lakey, A. Zuend, J. P. D. Abbatt and M. Shiraiwa, *Proc.*
Natl. Acad. Sci. U. S. A., 2019, **116**, 11658–11663.
- 928 Zhou, S., M. Shiraiwa, R. D. McWhinney, U. Pöschl and J. P. D. Abbatt, *Faraday Discuss.*,
2013, **165**, 391–406.
- 930 Zobrist, B., V. Soonsin, B. P. Luo, U. K. Krieger, C. Marcolli, T. Peter and T. Koop, *Phys.*
Chem. Chem. Phys., 2011, **13**, 3514–3526.
- 932 Zuend, A., C. Marcolli, A. M. Booth, D. M. Lienhard, V. Soonsin, U. K. Krieger, D. O.

934 Topping, G. McFiggans, T. Peter and J. H. Seinfeld, *Atmos. Chem. Phys.*, 2011, **11**,
9155–9206.

Zuend, A., C. Marcolli, B. P. Luo and T. Peter, *Atmos. Chem. Phys.*, 2008, **8**, 4559–4593.

936